

Camera-Sampling Field and Its Applications

Ping-Hsien Lin and Tong-Yee Lee, *Member, IEEE*

Abstract—In this paper, we propose a novel vector field, called a camera-sampling field, to represent the sampling density distribution of a pinhole camera. We give the derivation and discuss some essential properties of the camera-sampling field, including flux, divergence, curl, gradient, level surface, and sampling patterns. This vector field reveals camera-sampling concisely and facilitates camera sampling analysis. The usage for this vector field in several computer graphics applications is introduced, such as determining the splat kernel for image-based rendering, texture filtering, mipmap level selection, level transition criteria for LOD, and LDI-construction.

Index Terms—Camera-sampling field, image-based rendering (IBR), layered depth image (LDI), level of detail (LOD), splatting.

1 INTRODUCTION

CONVENTIONALLY, the term “camera model” in computer graphics and computer vision refers to a perspective projection matrix that maps a 3D world space onto a 2D image space. This model has worked very successfully in many domains relating directly to perspective geometry. In computer graphics, we use it to render a scene onto an image. In computer vision, it is used to derive many perspective projection geometry properties for scene reconstruction. However, this camera model does not concisely reveal the camera sampling properties. Camera sampling analysis can play an important role in many applications such as splatting for image-based rendering [1], [2], [3], [4], [5] or volume rendering [6], [7], [8], [9], texture filtering [10], [11], level transition criterion for LOD [12], and sampling quality evaluation for cameras with scenes [13], [14], [15]. To the best of our knowledge, because there is no general model to describe camera sampling, these works are sometimes treated independently and similar relations are derived. The purpose of this paper is to propose a general model for camera sampling to relate and solve many important computer graphics applications.

Chen and Williams [16] wrote a pioneering paper on image-based rendering that used several reference images to regenerate a novel view image. Because of the difference in sampling between the reference and novel views, some holes were left on the novel view images. Several studies focused on how to apply the splatting technique to improve the image quality and maintain a reasonable rendering speed. To estimate the splat size on a regenerated image, Shade et al. [1] and Chang et al. [2] used a simplified splat size decision equation according to perspective geometry. Similarly, Rusinkiewicz and Levoy [3] used the projected diameter of a sphere in the bounding sphere hierarchy tree.

Pfister et al. [4] used the longest projected diagonal of blocks in a LDC tree. Because splatting and texture filtering are the same problem, but in opposite ways, under the elliptical weighted average (EWA) filter framework described by Heckbert [11], Zwicker et al. [5] recently proposed a screen space EWA surface splatting. The EWA filter was derived based on an $\mathbb{R}^2 \rightarrow \mathbb{R}^2$ perspective mapping and the resampling theory in DSP (digital signal processing). The EWA filter is precise, but with a high computation cost. Zwicker et al. [9] used a similar concept to propose an EWA volume splatting technique for nonspherical kernels.

Another problem that accompanies image-based rendering is that, given a scene, how many reference images are needed and where should these reference images be placed such that the regenerated novel view images would possess better quality and fewer holes. We call this problem sampling optimization. This problem can be divided into two subproblems: visibility analysis and sampling quality analysis. Visibility analysis is an NP problem and was always solved using brute-force algorithms [13], [14], [17]. We will not deal with visibility analysis in this work. Sampling quality analysis is usually decided using some information between the scene primitives and camera, including the distance, projection area, viewing direction, and so on. In this paper, we introduce some factors to evaluate the sampling quality using the camera-sampling field. Additionally, sampling quality analysis is useful for applications that need to evaluate how well a camera shoots a scene, such as the level transition criterion for LOD and mipmap level selection [18].

In this study, the sampling density distribution of a pinhole camera was modeled according to the property that the pinhole camera samples on an image plane are uniform. A vector field is then used to represent this sampling density distribution. We proposed this idea and derivations in [19]. In this paper, we extend this preliminary result and draw new derivations and concepts. This novel representation can facilitate the sampling analysis for many computer graphics applications. Many applications can potentially benefit from camera sampling analysis, including the splatting kernel for IBR, texture filtering, mipmap level

• The authors are with the Computer Graphics Group/Visual System Laboratory, Department of Computer Science and Information Engineering, National Cheng-Kung University, No. 1, Ta-Hsueh Road, Tainan 701 Taiwan, ROC.

E-mail: phlin@vision.csie.ncku.edu.tw, tonylee@mail.ncku.edu.tw.

Manuscript received 23 June 2003; revised 23 Nov. 2003; accepted 8 Dec. 2003.

For information on obtaining reprints of this article, please send e-mail to: tcvg@computer.org, and reference IEEECS Log Number TVCG-0046-0603.

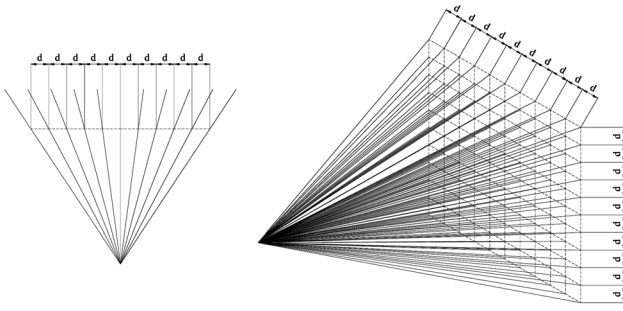


Fig. 1. Sampling line distribution of a camera in 2D and 3D.

selection, LOD transition criterions, LDI-construction (see Section 4), and so on. The mathematical properties of this vector field, such as flux, divergence, curl, gradient, level surfaces, and the sampling pattern's aspect ratio, can be further used to analyze the sampling in detail. The remainder of this paper is organized as follows: In Section 2, a formal derivation of the 2D and 3D camera-sampling field is given. Some essential mathematical properties are discussed in Section 3. In Section 4, several applications are illustrated and discussed. Our conclusion and future works are presented in Section 5.

2 CAMERA-SAMPLING FIELD

In this section, a formal derivation of the camera-sampling field is given. For a camera positioned in space, we say that the camera creates a sampling field within its field of view (FOV). This field describes the sampling density distribution of a pinhole camera. In Fig. 1, we represent both the 2D and 3D camera sampling fields using sampling lines. Each sampling line radiates from the center of projection (COP) of a camera. The higher the line density in Fig. 1, the higher the sampling density. First, we define the sampling density.

Definition 1. *The sampling density at a position in a specified direction is the number of samples per unit area (or per unit length in the 2D case) that is centered on that position and perpendicular to the specified direction.*

For a single camera, the sampling varies smoothly and its sampling lines never intersect one another except for the COP. We can use a vector to represent the sampling density by assigning the vector length as the density and the vector direction as the specified direction. The camera-sampling field is formally defined below.

Definition 2. *A camera-sampling field is a vector field that describes the sampling density distribution of a pinhole camera in the direction pointing toward the COP.*

In the following, an italic letter (a or A) represents a scalar, a bold small letter (\mathbf{a}) represents a vector, and $a \equiv |\mathbf{a}|$.

2.1 2D Camera-Sampling Field Derivation

Fig. 2 illustrates how a 2D camera-sampling field is derived. The angle between the *optical axis* of the camera (y -axis in Fig. 2) and a sampling line passing a point (x, y) is denoted as $\theta(x, y)$ and $\theta(x, y) = \tan^{-1}(x/y)$. First, $c^{II}(0, y)$ denotes the 2D camera-sampling field at point $(0, y)$ on the optical axis.

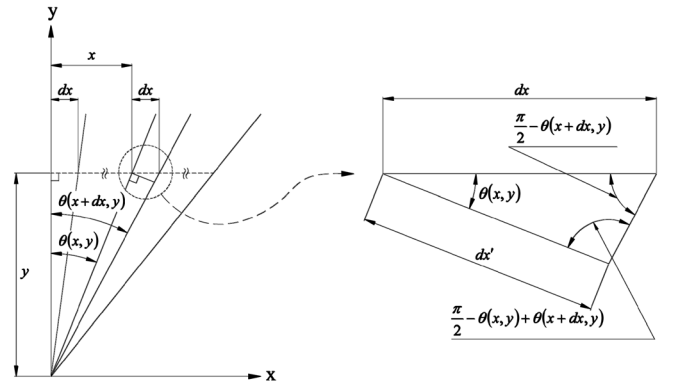


Fig. 2. Derivation of 2D camera-sampling field.

Because of the divergence in the sampling lines, the sampling density drops linearly as the distance from the COP increases. Therefore, along the optical axis, the sampling density is in inverse proportion to the distance from the COP.

$$c^{II}(0, y) = -\frac{C^{II}}{y}\mathbf{j}, \quad (1)$$

where C^{II} is the 2D camera-sampling constant and \mathbf{i} and \mathbf{j} are unit vectors in the x and y axes, respectively.

Because the sampling density on the image plane in the y direction is $-\mathbf{j}$ (one sampling per unit length), from (1), we can evaluate C^{II} :

$$\begin{aligned} c^{II}(0, f) &= -\frac{C^{II}}{f}\mathbf{j} = -\mathbf{j} \\ \Rightarrow C^{II} &= f = \frac{res}{2} \cot\left(\frac{fov}{2}\right). \end{aligned} \quad (2)$$

In (2), f is the focal length and res is the image resolution. By comparing the sampling density at point $(0, y)$ and (x, y) , we can obtain the strength of the camera-sampling field at any point (x, y) , as shown in (3) (for details, see the Appendix i).

$$\begin{aligned} \frac{c^{II}(x, y)}{c^{II}(0, y)} &= \lim_{dx \rightarrow 0} \frac{dx}{dx'} \\ \Rightarrow c^{II}(x, y) &= \frac{f\sqrt{x^2 + y^2}}{y^2}. \end{aligned} \quad (3)$$

Multiplying (3) by the unit direction vector

$$\left(-\frac{x\mathbf{i} + y\mathbf{j}}{\sqrt{x^2 + y^2}}\right),$$

we have a representation of the 2D camera-sampling field as:

$$c^{II}(x, y) = \begin{cases} -f\frac{x\mathbf{i} + y\mathbf{j}}{y^2}, & (x, y) \text{ within FOV} \\ 0, & \text{otherwise.} \end{cases} \quad (4)$$

2.2 3D Camera-Sampling Field Derivation

Considering a point $P = (x, y, z)$ within the FOV of a camera, point P is associated with three planes E_0 , E_1 , and E_2 (see Fig. 3), where E_0 is parallel to the image plane, E_1 passes through P 's vertical line on plane E_0 and the COP, and E_2 passes through P 's horizontal line on plane E_0 and

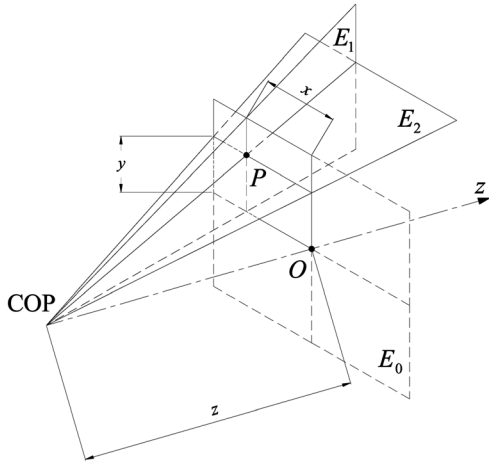


Fig. 3. 3D camera sampling field derivation.

the COP. To find the 3D camera-sampling field at P , the 2D camera-sampling fields on E_1 and E_2 are found first. The 3D camera-sampling field is then computed according to the included angle between E_1 and E_2 .

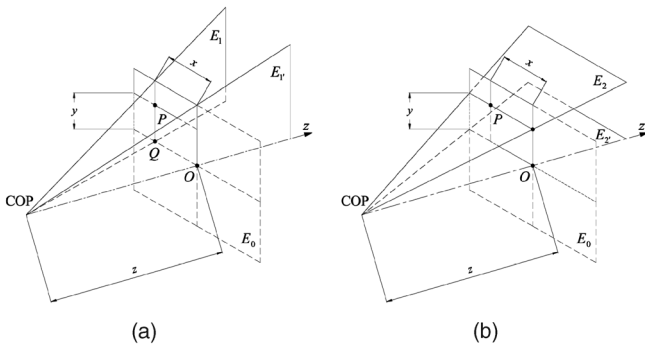
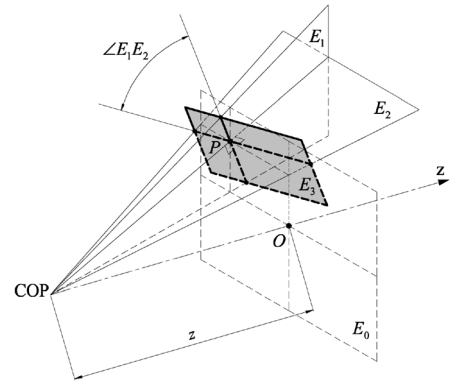
In Fig. 4a, there are two planes E_1 and $E_{1'}$. The strength of the 2D camera-sampling field at point O (on the optical axis) on $E_{1'}$ is $c^{II\{E_{1'}\}}(O) = f \frac{1}{z}$. Because the strength of the 2D sampling field at point Q on E_1 will be equal to that at O on $E_{1'}$, we have $c^{II\{E_1\}}(Q) = c^{II\{E_{1'}\}}(O) = f \frac{1}{z}$. According to (3), the strength of the 2D camera-sampling field at point P on E_1 is

$$c^{II\{E_1\}}(P) = f \frac{\sqrt{x^2 + y^2 + z^2}}{z\sqrt{x^2 + z^2}}$$

(see the Appendix, ii) and, similarly,

$$c^{II\{E_2\}}(P) = f \frac{\sqrt{x^2 + y^2 + z^2}}{z\sqrt{y^2 + z^2}}.$$

Now, let us consider a plane E_3 that is perpendicular to the sight ray, as shown in Fig. 5. Because the sampling density at point P in the direction pointing to COP is the reciprocal of the area per sample on this plane, we can get (for details, see the Appendix, iii):


 Fig. 4. (a) Plane E_1 and $E_{1'}$. (b) Plane E_2 and $E_{2'}$.

 Fig. 5. Plane E_1 , E_2 , and E_3 . E_3 is perpendicular to the sight ray (or is perpendicular to both E_1 and E_2 planes).

$$c^{III}(P) = \frac{1}{\frac{1}{c^{II\{E_1\}}(P)} \frac{1}{c^{II\{E_2\}}(P)} \sin(\angle E_1 E_2)} = f^2 \frac{\sqrt{x^2 + y^2 + z^2}}{z^3}. \quad (5)$$

Multiplying (5) by the unit direction vector

$$\left(-\frac{x\mathbf{i} + y\mathbf{j} + z\mathbf{k}}{\sqrt{x^2 + y^2 + z^2}} \right),$$

we have the 3D camera-sampling field representation as:

$$\mathbf{c}^{III}(x, y, z) = \begin{cases} -f^2 \frac{x\mathbf{i} + y\mathbf{j} + z\mathbf{k}}{z^3}, & (x, y, z) \text{ within FOV} \\ \mathbf{0}, & \text{otherwise.} \end{cases} \quad (6)$$

3 PROPERTIES OF CAMERA-SAMPLING FIELD

In this section, several properties of the camera-sampling field will be discussed. The focus is on the properties of a 3D camera-sampling field and, hence, the superscript III is hereafter omitted in this paper. The 2D camera-sampling field also possesses the corresponding properties in two dimensions.

Using the coordinates settings shown in Fig. 6, we can rewrite (6) under spherical coordinates as:

$$\mathbf{c}(\rho, \theta, \phi) = \begin{cases} -\frac{f^2}{\rho^2 \cos^3 \phi} \mathbf{u}_\rho, & (\rho, \theta, \phi) \text{ within FOV} \\ \mathbf{0}, & \text{otherwise.} \end{cases} \quad (7)$$

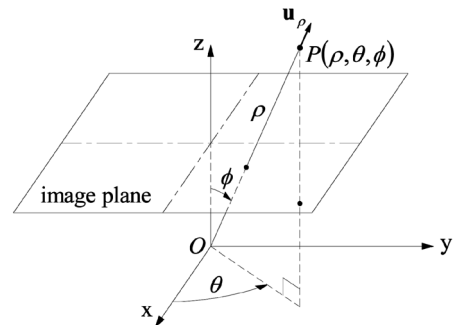


Fig. 6. The relationship between the Cartesian and spherical coordinates.

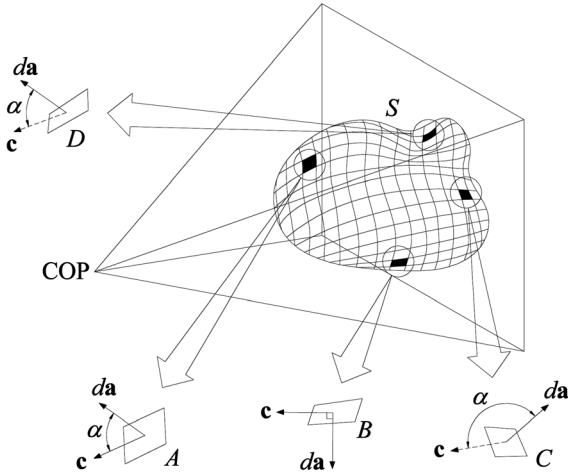


Fig. 7. The camera sampling flux ($\mathbf{c} \cdot d\mathbf{a}$) for the surface element A is positive: $\mathbf{c} \cdot d\mathbf{a} = 0$ ($\alpha = 90^\circ$) for B ; for both C and D , the camera sampling fluxes are zero because they are not visible. (C is backface and D is occluded.)

3.1 Camera-Sampling Flux

The flux of the camera-sampling field, *camera-sampling flux*, is defined as:

$$\Phi_C = \int_{S_v} \mathbf{c} \cdot d\mathbf{a}, \quad (8)$$

where S_v stands for visible surface.

There is a distinct difference between the flux definition of the camera-sampling field and other vector fields, like an electric field. That is, for a given camera, the surface integral of the camera-sampling flux is performed only on visible surfaces (see Fig. 7). For a camera and scene surface, the number of samples is proportional to Φ_C .

3.2 Divergence and Curl

The divergence of a camera-sampling field is:

$$\text{div } \mathbf{c} = \nabla \cdot \mathbf{c} = -f^2 \left(\frac{\partial(x/z^3)}{\partial x} + \frac{\partial(y/z^3)}{\partial y} + \frac{\partial(1/z^2)}{\partial z} \right) = 0. \quad (9)$$

Consider a solid angle spanned by a pyramid from a camera's COP (see Fig. 8). There are two curved surface patches S_1 and S_2 inside the pyramid. S_3, S_4, S_5 , and S_6 are the four planes of this pyramid between S_1 and S_2 , and $S_1 \sim S_6$ define a closed bounded region V . I is the projected area of both S_1 and S_2 on the image plane. According to the

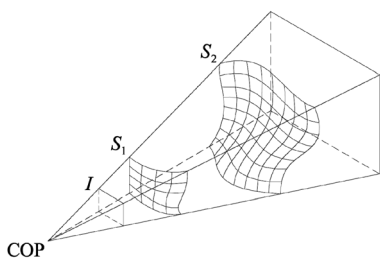


Fig. 8. A solid angle spanned by a pyramid from COP.

Gauss' divergence theorem [20], within the closed bounded region V , we have:

$$\oint_{\{S_1+S_2+S_3+S_4+S_5+S_6\}} \mathbf{c} \cdot d\mathbf{a} = \int_V \nabla \cdot \mathbf{c} d\tau = 0. \quad (10)$$

On the planes S_3, S_4, S_5 , and S_6 , $\mathbf{c} \cdot d\mathbf{a} = 0$ (therefore $\mathbf{c} \perp d\mathbf{a}$), so we have

$$\oint_{S_1} \mathbf{c} \cdot d\mathbf{a} + \oint_{S_2} \mathbf{c} \cdot d\mathbf{a} = 0. \quad (11)$$

From (11), we can conclude that under an identical solid angle, all surface patches that can cross all of the spans in this solid angle will have an equal camera sampling flux. Moreover, since the camera sampling flux on the image plane is equal to the projected area on the image plane (because on image plane $|\mathbf{c} \cdot d\mathbf{a}| = 1$), we can conclude:

Property 1. *The camera sampling flux of a scene surface with respect to a camera is equal to its projection area on the camera's image plane.*

This property implies that, without considering occlusion, we can evaluate a surface projection area directly on the surface without projecting it. Therefore, it is possible to perform sampling analysis on scene surface in detail, even within a single triangle. In Section 4, we will use a camera-sampling field to define the more precise factors for evaluating how well a surface is sampled by a camera.

The curl of the camera-sampling field is:

$$\text{curl } \mathbf{c} = \nabla \times \mathbf{c} = -3C \frac{y}{z^4} \mathbf{i} + 3C \frac{x}{z^4} \mathbf{j} \quad (\text{Cartesian coordinates})$$

or

$$\nabla \times \mathbf{c} = \frac{3C \sin \phi}{\rho^3 \cos^4 \phi} \mathbf{u}_\theta \quad (\text{spherical coordinates}). \quad (12)$$

From (12), we know that the curl direction is always parallel to \mathbf{u}_θ as shown in Fig. 9a. Fig. 9b shows a profile passing through the optical axis to illustrate the sampling line distribution. In this figure, the curl direction at P points inward the paper (i.e., clockwise). Consider the vicinity of point P , the nonzero curl at P means that the sampling density on the right side of P is denser than that on left side. The curl value indicates the increasing sampling density rate along ϕ .

The curl can be used to evaluate how variant the sampling density is around a location. The more serious the sampling variance, the poorer the sampling. Therefore, a curl can be one of the factors used to evaluate how well a surface is sampled by a camera. Another potential use is to shear the splat kernel on an image. After a perspective projection, the splat kernel is no longer symmetrical on that image.

3.3 Level Surface and Gradient

The level surface of the strength function of the camera-sampling field is:

$$|\mathbf{c}| \equiv c = \frac{f^2}{\rho^2 \cos^3 \phi} = k, \quad (13)$$

where k is a constant.

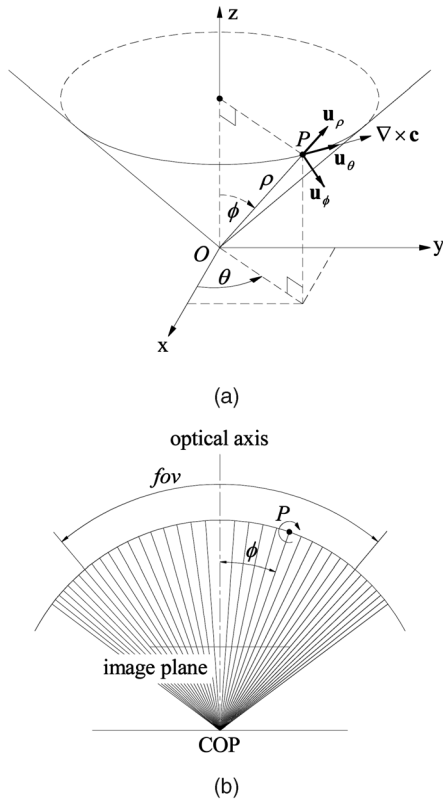


Fig. 9. (a) The curl ($\nabla \times \mathbf{c}$) of a camera-sampling field in spherical coordinates. (b) The sampling density increases as ϕ increases for a fixed ρ .

The gradient of the strength function of the camera-sampling field is:

$$\nabla c = -\frac{2C}{\rho^3 \cos^3 \phi} \mathbf{u}_\rho + \frac{3C \sin \phi}{\rho^3 \cos^4 \phi} \mathbf{u}_\phi. \quad (14)$$

In Fig. 10, we show a level surface and gradient profile that passes through the optical axis. On each level surface, every point has an equal sampling density. Two objects (for example, the object A and B in Fig. 10) at the same level surface will have similar sampling conditions. Their projection sizes will also be similar. Therefore, the sampling density can be a level transition criterion for several applications in computer graphics such as view-independent LOD. Note

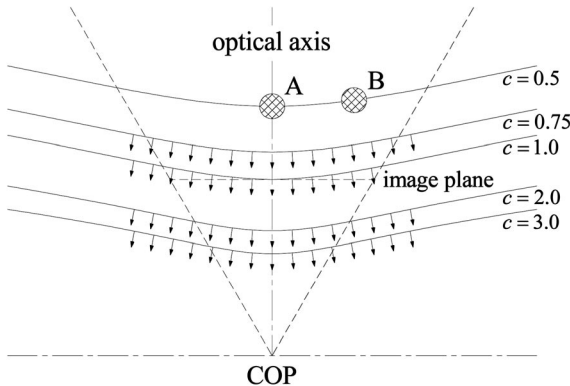


Fig. 10. A level surface and gradient profile of the camera-sampling field.

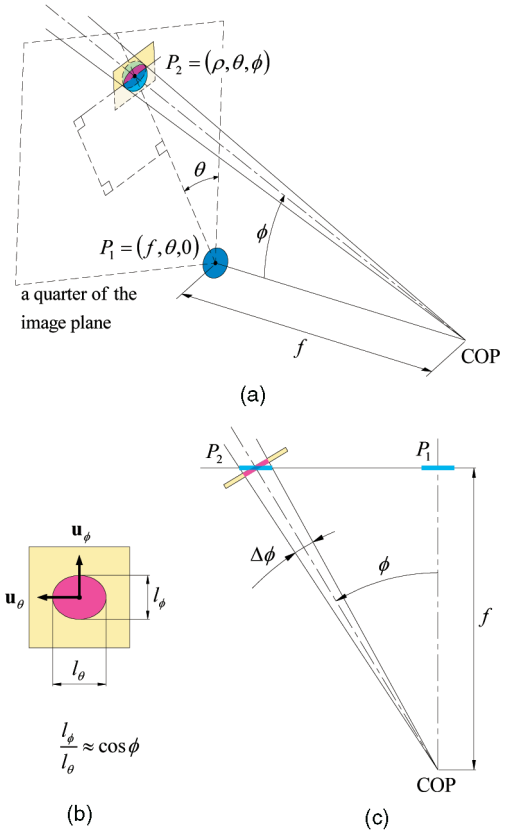


Fig. 11. Sampling pattern illustration. f is the focal length and P_1 is the sampling on the image center.

that the gradient direction does not point toward the COP except on the optical axis (see the arrows in Fig. 10). This feature could be potentially helpful in sampling optimization since the gradient is the direction in which the sampling density increases fastest.

3.4 Aspect Ratio of Sampling Pattern

We have introduced some properties derived directly from the camera-sampling field. Note that the camera-sampling field is a vector field. It can characterize only the sampling densities and sampling directions. However, there is one more important thing for sampling: the sampling patterns. Sampling patterns could be very complicated. For simplification and representability, we use aspect ratios to characterize sampling patterns. Thus, the sampling patterns can be thought of as ellipses. The minor axis ratio with the major axis of an ellipse stands for the sampling pattern aspect ratio.

The samples are distributed in square-grid patterns on the image plane. In Section 2, a continuous vector field is used to describe the camera sampling based on the assumption that the sampling density on the image plane is uniform. This implies that the sampling distribution on the image plane is isotropic. Thus, the sampling pattern aspect ratio on the image plane is always unity. In Fig. 11a, we used two blue circles to represent two samples on the image plane ($P_1 = (f, \theta, 0)$ and $P_2 = (\rho, \theta, \phi)$), where f is the focal length and $\rho \cos \phi = f$. At P_1 , the sampling direction is perpendicular to the image plane. The sampling pattern

aspect ratio in this direction ($\phi = 0$) is the same as that on the image plane. At P_2 , the sampling direction and the image normal share an included angle ϕ . Thus, the camera field sampling pattern in this direction should be obtained by perspective projecting the sampling pattern onto the image plane to a plane (the yellow quadrilateral in Fig. 11a) perpendicular to this direction. Fig. 11b shows the front view of this plane with the sampling pattern on it. Fig. 11c shows a profile passing through P_1 , P_2 , and COP (a plane with fixed θ). When the sample on the image plane approximates infinitesimal (this means the camera sampling model approximates continuous), the perspective projection approximates a parallel projection in this sampling direction. This parallel projection compresses the sampling pattern in the \mathbf{u}_ϕ direction with a factor of $\cos \phi$. Therefore, we define the sampling pattern aspect ratio as the length ratio of the sampling pattern in the \mathbf{u}_ϕ and \mathbf{u}_θ direction as shown in Fig. 11b. This aspect ratio is equal to $\cos \phi$. Because the solid angle spanned by each sample on the image plane is very small, the error produced by this approximation is insignificant (see the splatting kernel analysis in Section 4). When the aspect ratio is smaller than 1, the lower the aspect ratio, the less uniform the sampling. Therefore, the sampling pattern aspect ratio can be a criterion for judging the sampling quality. It can also be used to analyze the shape of a splat kernel, as will be discussed in Section 4.

3.5 Addition of Camera-Sampling Field

In force and electrical fields, the lines of force or field lines are imaginary. They are only used to visualize the abstract continuous field concept. The vector addition operation can be applied perfectly to such continuous fields. However, camera sampling is discrete. Each sampling line indeed exists and corresponds to a pixel on the image plane. In this paper, we apply vector addition to compose multiple fields. Though not perfectly, it is still meaningful for some camera sampling applications.

A compound camera-sampling field represents the maximal compound sampling density and its direction. This means that the compound field will produce maximal sampling density in this direction without concern for the scene surfaces. In the LDI-construction problem (see Section 4), this tells us that we can use a camera that provides the same sampling as the compound field to sample the reference depth images and obtain an approximate sampling without considering about the visibility. Using these concepts, we can clarify the LDI-construction problem and find the best resampling position for a LDI (see Section 4).

4 APPLICATIONS OF CAMERA-SAMPLING FIELD

In this section, we introduce some camera-sampling field applications. We can see that the proposed camera-sampling field can be used successfully in many kinds of applications in computer graphics. Note that, in Sections 2 and 3, we depicted the camera-sampling field in the camera's local coordinates. In the following, all vectors are expressed in global world coordinates.

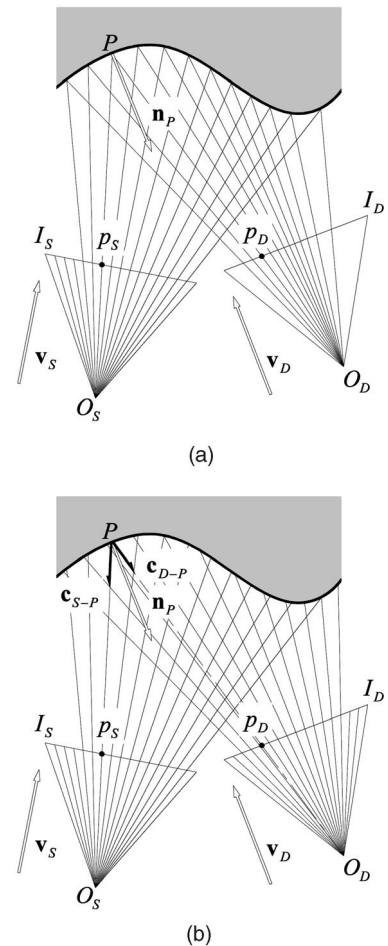


Fig. 12. Sampling analysis for image-based rendering.

4.1 Local Sampling Analysis

4.1.1 Splatting Kernel for Image-Based Rendering

Fig. 12a shows a splatting illustration for image-based rendering. For a given scene, the geometric surfaces are sampled using a source camera O_S . These samples are then projected onto the image plane of the destination camera O_D . The splat size is inversely proportional to the projection density of these samples on the destination image. To obtain this projection density, we merely need to compare the sampling density of the source and destination cameras on the scene surface. Therefore, the splat size can be calculated using (see Fig. 12b) (for comparison with [1], please refer to [21]):

$$\text{splat size}(p_D) = \frac{c_{D-P} \cdot \mathbf{n}_P}{c_{S-P} \cdot \mathbf{n}_P}. \quad (15)$$

In [4], a sample point is called a "surfel," represented by an oriented disk on a surface. We can calculate the splat size using (15) by replacing $c_{S-P} \cdot \mathbf{n}_P$ with the sampling density of the sample point on the scene surface. Fig. 13a shows a splat whose size has been determined on the image plane. There are two factors that affect the shape of a splat kernel. The first factor is the orientation of the surfel's normal. A surfel is first parallel projected onto a plane perpendicular

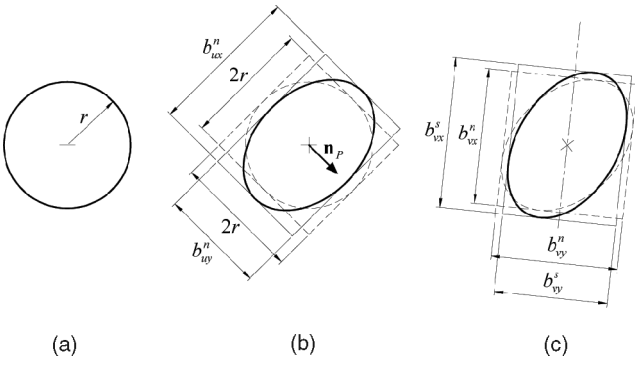


Fig. 13. Shape decision of a splat kernel for uniformly sampled points. The symbol b_{ux}^n represents the bounding length in the x -axis of a coordinate u whose y -axis is parallel to the project normal \mathbf{n}_p . v is a coordinate whose x -axis is parallel to the straight line passing through the image-center and the projection of sample point.

to a sight ray. This shape is then drawn on the image plane according to the orientation of the projected normal as shown in Fig. 13b ($\frac{b_{vy}^n}{b_{ux}^n} = \text{dot}(\mathbf{n}, \text{sight ray})$). To maintain the splat's area, we need $\frac{b_{ux}^s b_{vy}^s}{4r^2} = 1$. The second factor is the aspect ratio of the sampling pattern. It stretches the shape along the radial direction from the image-center with a factor of $\frac{1}{\cos \phi}$, as shown in Fig. 13c ($\frac{b_{vy}^s/b_{vy}^n}{b_{ux}^s/b_{ux}^n} = \cos \phi$ and $\frac{b_{ux}^s b_{vy}^s}{b_{ux}^n b_{vy}^n} = 1$). This approach can easily be implemented by stretching a circular texture on the image plane.

Fig. 14 shows the splat kernels of three sample points using two different methods. Fig. 14a is the correct perspective surfel projection implemented using oriented circular textured triangles in a 3D space [3]. Fig. 14b is the proposed method that stretches a circular texture on a 2D image. Fig. 14c shows the difference between these two approaches. We can see that, even in such an extreme case (large projection size and off-center position), the differences are not apparent. Fig. 15a shows an original triangle model with the sample points on the surface. Fig. 15b is generated using the proposed splat kernel decision method. Each kernel is implemented by stretching a circular Gaussian texture on a 2D image plane. We adopted a two-pass rendering pipeline that produces the depth buffer in the first pass and culls the visible splats in the second pass. All of the visible splat kernels were then accumulated on the color buffer following a normalization procedure. We can see that these two images are quite similar. More precise splat analysis is left for the future. For example, a truly perspective projection splat kernel is not symmetrical.

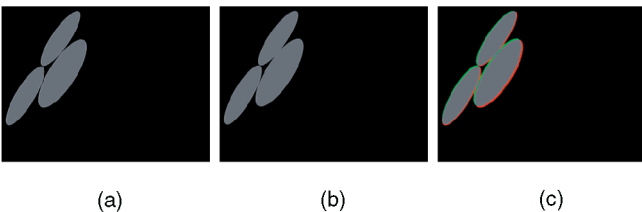


Fig. 14. Splat kernel comparison. (a) Correct perspective projection. (b) Proposed method. (c) Difference between (a) and (b). The green areas are parts of (a), the red areas are parts of (b), and the gray areas are the intersections between (a) and (b).

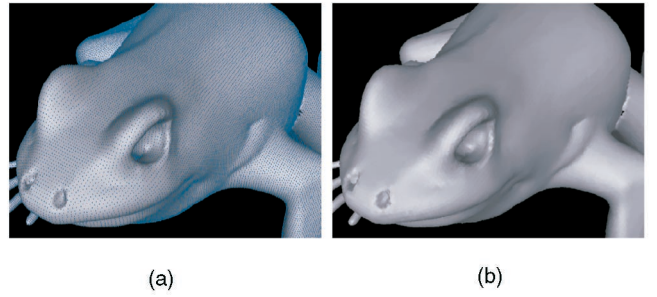


Fig. 15. Splatting using the proposed splat kernel decision method. (a) Original triangle model with sample points (colored in blue). (b) Splatting with the proposed splat kernel decision method.

The kernel content should be sheared a little bit to mimic a perspective projection. We think that the curl of the camera-sampling field is the factor responsible for this affect.

4.1.2 Texture Filtering

Texture filtering is the same problem as splatting but in the opposite way. An approach analogous to the splatting technique described above can be applied to determine the filter kernel and obtain the filtered color.

4.1.3 Projection Factor for a Small Surface Fragment

In [15], a projection factor for a small surface fragment (s) was defined to obtain the probability density function for sample point selection. This projection factor is equivalent to the camera sampling density on a surface.

$$proj(s) = \mathbf{c} \cdot \mathbf{n}, \quad (16)$$

where \mathbf{n} is the normal of the surface fragment s .

4.1.4 Mipmap Level Selection

For the filter dimension for perspective texture mapping, Heckbert [22] suggested an equation that approximated the square root of the projection area cast from a pixel onto the surface (texture space). Williams [18] adopted this as the filter's diameter for each mipmap level. The mipmap level selection is just the inverse problem to the above projection factor evaluation problem. Therefore, we can use the square root of the reciprocal of (16) ($\sqrt{\frac{1}{\mathbf{c} \cdot \mathbf{n}}}$) to calculate the filter dimension to determine the mipmap level. This method is more precise but with a higher cost.

4.1.5 Level Transition Criterion for View-Dependent LOD

The projection factor evaluated using (16) can be adopted for level transition criterion of view dependent LOD. The sampling pattern aspect ratio and camera-sampling field curl can be one of the criteria. The sampling pattern aspect ratio means the pattern regularity of this sample. The curl describes the variation in sampling density around a location. Moreover, the factors described in the next section ((17) and (18)) can be evaluated on a surface patch for the same purpose with more precise analysis, but with higher computation cost.

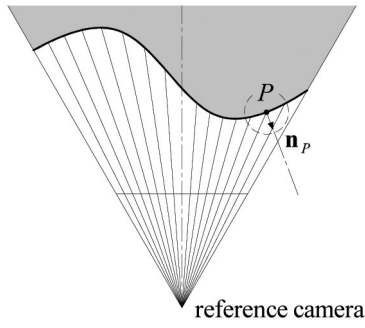


Fig. 16. LDI-construction from one reference image.

4.2 Global Sampling Analysis

4.2.1 Sampling Optimization

A research issue in IBR is that, given a scene, how many reference images are needed and where should these reference images be placed such that the regenerated images possess better quality. In this paper, we only discuss the sampling quality issue. With the camera-sampling field, we can define more precise factors to describe how well a camera shoots a scene. Equations (17) and (18) are the mean and standard deviation of the camera sampling flux through the scene surfaces. We prefer higher mean and lower deviation. These factors can be evaluated directly using the numerical integral on the 3D surface patches.

$$\mu_f = \frac{\int_{S_v} \mathbf{c} \cdot d\mathbf{a}}{\int_{S_v} 1 da} = \frac{\Phi_C}{\text{Area}(S_v)}, \quad (17)$$

$$\sigma_f = \left(\frac{\int_{S_v} (\mathbf{c} \cdot \mathbf{n} - \mu_f)^2 da}{\int_{S_v} 1 da} \right)^{\frac{1}{2}}, \quad (18)$$

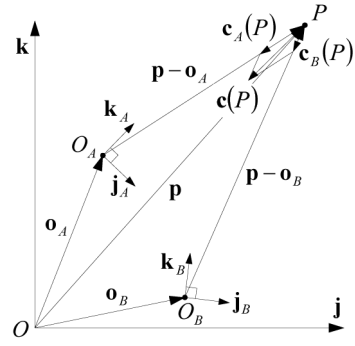
where S_v denotes a visible surface and \mathbf{n} is the surface normal.

4.2.2 Level Transition Criteria for View-Independent LOD

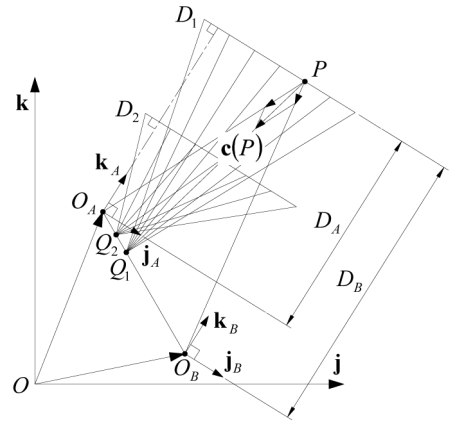
The most intuitive LOD level transition criteria are distance, viewing direction, and the object projection size. The camera-sampling field can offer other factors, such as the sampling density, the aspect ratio of the sampling patterns, camera-sampling field curl, and the factors defined in (17) and (18). All of these factors are meaningful, as we have explained above.

4.2.3 LDI-Construction

An LDI is constructed by projecting several reference depth images to a certain position (LDI's COP). Shade et al. [1] did not mention explicitly how they determined the LDI's COP. Chang et al. [2] stored an LDI for each octree cell. Popescu et al. [23] stored an LDI for each portal in an architecture. Each portal's LDI is constructed by warping $2n + 1$ reference images on a semicircle in front of the portal to the middle one. All of these works used an intuitive method to determine the LDI's COP. We defined the LDI-construction problem as: When reference images are available, where should the LDI's COP be set and what should the LDI resolution be such that the LDI could most properly



(a)



(b)

Fig. 17. LDI-construction illustration. These illustrations are pictured in 2D while our equations are in 3D. (a) Two arbitrary cameras and their composed field at P . (b) The sampling condition of two parallel cameras.

represent all of the reference images? Here, "properly" implies the potential to generate higher quality new views.

Let us consider the simplest case first, constructing a LDI from one reference image, as shown in Fig. 16. We say that the reference camera creates a camera sampling field within its field of view. When we only consider the geometric properties around the vicinity of a point P , the best resampling position should be located along P 's normal direction. Along this direction, we can sample this area using a lower sampling density (or lower image resolution). However, when considering all of the scenes, the best resampling position should be the same as the reference camera. This is because, only at this position can a camera be used to sample the scene with the same sampling density everywhere on the scene surfaces (or create the same camera sampling field as the reference camera).

Consider two cameras in a scene (Fig. 17a). At a position P , the compound field is $\mathbf{c}(P) = \mathbf{c}_A(P) + \mathbf{c}_B(P)$. A line passing P and parallel to $\mathbf{c}(P)$ can be written as:

$$\begin{aligned} & \mathbf{p} + s\mathbf{c}(P) \\ &= \mathbf{p} - s \left(f_A^2 \frac{\mathbf{p} - \mathbf{o}_A}{(\mathbf{R}_A \mathbf{k} \cdot (\mathbf{p} - \mathbf{o}_A))^3} + f_B^2 \frac{\mathbf{p} - \mathbf{o}_B}{(\mathbf{R}_B \mathbf{k} \cdot (\mathbf{p} - \mathbf{o}_B))^3} \right), \end{aligned} \quad (19)$$

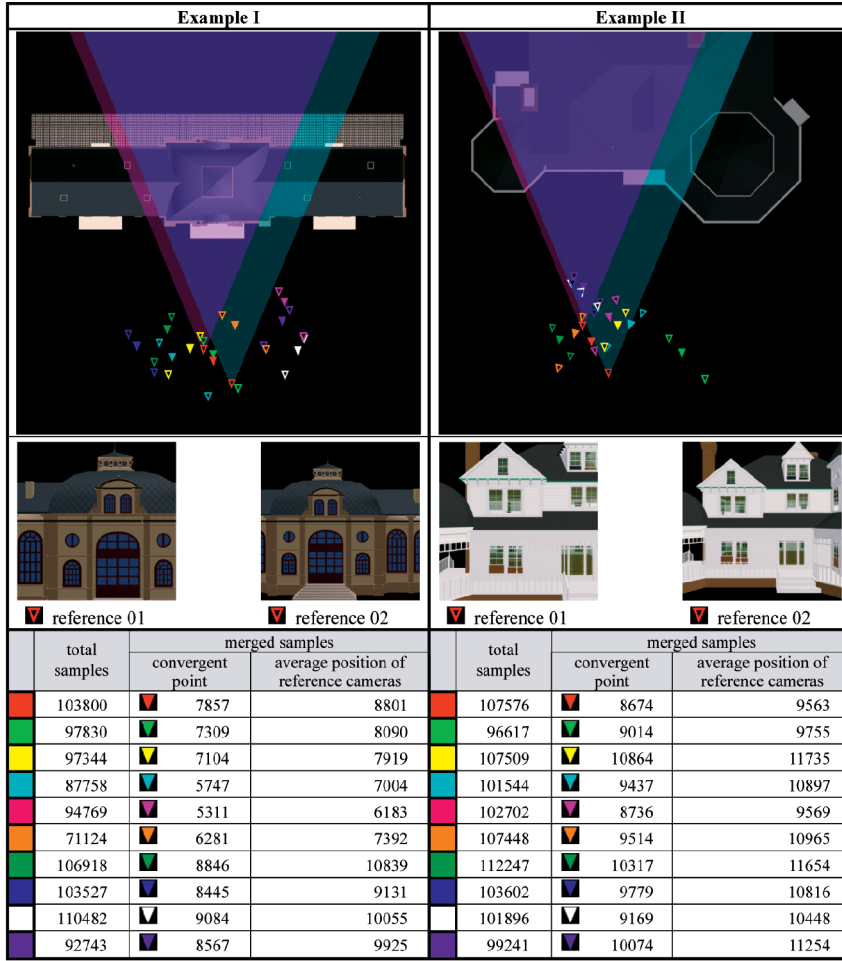


Fig. 18. Two comparisons of the LDI-construction from the convergent point and the average position. In each example, the first row image shows the top view of the scenes and 10 sets of camera configurations (each configuration has two reference cameras and one camera at a convergent point). The view frustums of the first set of cameras are also shown in the top view. The second row images show the first set of reference images. The number of total samples is counted by the samples inside the intersection of two reference view-frustums.

where s is a scale value. f_A and f_B are the focal lengths of cameras A and B . \mathbf{R}_A and \mathbf{R}_B are the rotation matrices that define the local coordinates for cameras A and B . $\mathbf{R}_A \mathbf{k} \equiv \mathbf{k}_A$ is the unit optical axis vector of camera A .

Assume that these two cameras are parallel. In this case, the denominators in (19) are fixed while P is located on a certain plane (says D_1 plane in Fig. 17b) that is perpendicular to the cameras' optical axes. Let $\mathbf{R}_A \mathbf{k} \cdot (\mathbf{p} - \mathbf{o}_A) = D_A$ and $\mathbf{R}_B \mathbf{k} \cdot (\mathbf{p} - \mathbf{o}_B) = D_B$, (19) can be rewritten as:

$$\left(1 - s \frac{D_B^3 f_A^2 + D_A^3 f_B^2}{D_A^3 D_B^3}\right) \mathbf{p} + s \frac{D_B^3 f_A^2 \mathbf{o}_A + D_A^3 f_B^2 \mathbf{o}_B}{D_A^3 D_B^3}. \quad (20)$$

Choose s to eliminate \mathbf{p} in (20). Equation (20) becomes:

$$\frac{D_B^3 f_A^2 \mathbf{o}_A + D_A^3 f_B^2 \mathbf{o}_B}{D_B^3 f_A^2 + D_A^3 f_B^2}. \quad (21)$$

This means that the compound fields at all positions on the D_1 plane would point to an identical point Q_1 located at

$$\frac{D_B^3 f_A^2 \mathbf{o}_A + D_A^3 f_B^2 \mathbf{o}_B}{D_B^3 f_A^2 + D_A^3 f_B^2}$$

(a point on $\overline{O_A O_B}$). We call this point the convergent point of the D_1 plane. Additionally, the sampling density at this plane in the plane's normal (or \mathbf{k}_A) direction is fixed and equal to

$$\frac{D_B^2 f_A^2 + D_A^2 f_B^2}{D_A^2 D_B^2}$$

(see the Appendix, iv). This means that, regardless of visibility, the reference cameras A and B form a camera-sampling-like field at the D_1 plane or we can say the sampling of cameras A and B on the D_1 plane is approximate to a specific camera. This camera's COP is located at the convergent point Q_1 and its camera-sampling constant is

$$\frac{(D_B^2 f_A^2 + D_A^2 f_B^2)^3}{(D_B^3 f_A^2 + D_A^3 f_B^2)^2}$$

(see the Appendix, v). Using this camera to resample the reference images, we can potentially create the high quality LDI representation.

Fig. 18 shows two examples of the comparison of the LDI-construction from the convergent point and the average position of the reference cameras. In each example, we randomly pick 10 sets of two parallel reference cameras. In example I, the viewing directions of all 10 sets of cameras point upward, whereas, in example II, some are not. The scenes are first sampled by the two reference cameras. Then, all the sampled points are reprojected to the convergent point or the average position of reference cameras to construct an LDI. Our analysis above is valid at the region that both reference cameras can see. Thus, in these two examples, we only focus on the region inside the intersection of two reference view-frustums. In the LDI-construction, improper resampling would cause many nearby samples to project to the same LDI pixel. In this case, the LDI [1] approach blends these samples together. This will cause a blur effect in LDI representation and the regenerated novel views. In these two examples of Fig. 18, the convergent point corresponds to a plane with the depth computed by averaging the depths of all of the samples. We can see that the resampling at the convergent point causes fewer samples to be merged into an LDI and, thus, we can keep more samples in the LDI representation than at the average position. Therefore, the convergent point is a better resampling position than the average position, as we expect.

5 CONCLUSION AND FUTURE WORKS

We presented a novel representation for modeling the sampling density distribution of a pinhole camera. This mathematical model facilitates the sampling analysis and clarifies the physical meaning of camera sampling. As illustrated and discussed in Section 4, this approach can be widely applied to many domains involving camera sampling. In this paper, we demonstrated some usages for this novel representation. Other mathematical properties of this model may be helpful for advanced analysis. For example, in general, the splat kernel should not be symmetrical. That is, the projection of a sample is not located at the center of the splat. We think that the curl can offer quantitative information about this problem. This analysis may not be feasible when considering rendering speed, but it can produce more precise output images. The LOD camera-sampling field applications were explained briefly and not illustrated by examples in this paper. We plan to apply the several criteria mentioned above to LOD techniques and quantify the results. Additionally, we discussed only the camera arrangement with the parallel view direction for LDI-construction problem. We will discuss more complicated and general reference camera arrangements in the near future. We are still investigating other new features and novel camera-sampling field applications.

APPENDIX

$$\begin{aligned}
 \text{(i)} \quad c^{II}(x, y) &= \lim_{dx \rightarrow 0} \left[\frac{dx}{dx'} c^{II}(0, y) \right] \\
 &= \lim_{dx \rightarrow 0} \left[\frac{\sin[\pi/2 - \theta(x, y) + \theta(x + dx, y)] C^{II}}{\sin[\pi/2 - \theta(x + dx, y)] y} \right] \\
 &= \lim_{dx \rightarrow 0} \left[\frac{\cos[\theta(x, y) - \theta(x + dx, y)] C^{II}}{\cos[\theta(x + dx, y)] y} \right] \\
 &= \lim_{dx \rightarrow 0} \left[\frac{\cos[\theta(x, y)] \cos[\theta(x + dx, y)] + \sin[\theta(x, y)] \sin[\theta(x + dx, y)] C^{II}}{\cos[\theta(x + dx, y)] y} \right] \\
 &= \lim_{dx \rightarrow 0} \left[\frac{C^{II}[y^2 + x(x + dx)]}{y^2 \sqrt{x^2 + y^2}} \right] = \frac{f \sqrt{x^2 + y^2}}{y^2}
 \end{aligned}$$

$$\begin{aligned}
 \text{(ii)} \quad c^{II\{E_1\}}(P) &= f' \frac{\sqrt{x^2 + y^2 + z^2}}{x^2 + z^2} \\
 &= f \frac{\sqrt{x^2 + z^2} \sqrt{x^2 + y^2 + z^2}}{z(x^2 + z^2)} \\
 &= f \frac{\sqrt{x^2 + y^2 + z^2}}{z \sqrt{x^2 + z^2}},
 \end{aligned}$$

where f' can be thought of as the focal length of the 2D camera on E_1 (Fig. 4a).

(iii) The normal of the planes E_1 and E_2 are $(z, 0, x)$ and $(0, z, y)$, respectively. Thus,

$$\sin(\angle E_1, E_2) = \sqrt{1 - \cos^2(\angle E_1 E_2)} = z \sqrt{\frac{x^2 + y^2 + z^2}{(x^2 + z^2)(y^2 + z^2)}}$$

$$\begin{aligned}
 \text{(iv)} \quad -\mathbf{c}(P) \cdot \mathbf{k}_A &= -\mathbf{c}_A(P) \cdot \mathbf{k}_A - \mathbf{c}_B(P) \cdot \mathbf{k}_B \\
 &= \frac{f_A^2}{D_A^2} + \frac{f_B^2}{D_B^2} = \frac{D_B^2 f_A^2 + D_A^2 f_B^2}{D_A^2 D_B^2}.
 \end{aligned}$$

(v) The depth (distance) from the D_1 plane to its convergent point is

$$\frac{D_B^3 f_A^2 D_A + D_A^3 f_B^2 D_B}{D_B^3 f_A^2 + D_A^3 f_B^2}.$$

Additionally, we know the sampling density at the D_1 plane in its normal direction. Therefore, we have:

$$\begin{aligned}
 \frac{C_{A+B}}{\left(\frac{D_B^3 f_A^2 D_A + D_A^3 f_B^2 D_B}{D_B^3 f_A^2 + D_A^3 f_B^2} \right)^2} &= \frac{D_B^2 f_A^2 + D_A^2 f_B^2}{D_A^2 D_B^2} \\
 \Rightarrow C_{A+B} &\equiv f_{A+B}^2 = \frac{(D_B^2 f_A^2 + D_A^2 f_B^2)^3}{(D_B^3 f_A^2 + D_A^3 f_B^2)^2} \\
 \Rightarrow f_{A+B} &= \frac{(D_B^2 f_A^2 + D_A^2 f_B^2)^{\frac{3}{2}}}{D_B^3 f_A^2 + D_A^3 f_B^2},
 \end{aligned}$$

where C_{A+B} and f_{A+B} are the camera-sampling constant and focal length of the new camera, respectively.

ACKNOWLEDGMENTS

The authors extend their thanks to the anonymous reviewers for their helpful comments. This paper is supported by the National Science Council, Taiwan, Republic of China, under contract No. NSC-92-2213-E-006-066 and NSC-92-2213-E-006-067.

REFERENCES

- [1] J. Shade, S. Gortler, L. He, and R. Szeliski, "Layered Depth Images," *Proc. SIGGRAPH '98*, pp. 231-242, July 1998.
- [2] C.F. Chang, G. Bishop, and A. Lastra, "LDI Tree: A Hierarchical Representation for Image-Based Rendering," *Proc. SIGGRAPH '99*, pp. 291-298, 1999.
- [3] S. Rusinkiewicz and M. Levoy, "QSPlat: A Multiresolution Point Rendering System for Large Meshes," *Proc. SIGGRAPH 2000*, pp. 343-352, July 2000.
- [4] H. Pfister, M. Zwicker, J. van Baar, and M. Gross, "Surfels—Surface Elements as Rendering Primitives," *Proc. SIGGRAPH 2000*, pp. 335-342, 2000.
- [5] M. Zwicker, H. Pfister, J. van Baar, and M. Gross, "Surface Splatting," *Proc. SIGGRAPH 2001*, pp. 371-378, 2001.
- [6] L. Westover, "Interactive Volume Rendering," *Proc. Chapel Hill Workshop Volume Visualization*, pp. 9-16, May 1989.
- [7] L. Westover, "Footprint Evaluation for Volume Rendering," *Proc. Siggraph '90*, vol. 24, pp. 367-376, 1990.
- [8] K. Mueller, T. Möller, J.E. Swan, R. Crawfis, N. Shareef, and R. Yagel, "Splatting Errors and Antialiasing," *IEEE Trans. Visualization and Computer Graphics*, vol. 4, no. 2, pp. 178-191, Apr.-June 1998.
- [9] M. Zwicker, H. Pfister, J. van Barn, and M. Gross, "EWA Volume Splatting," *Proc. IEEE Visualization 2001*, pp. 29-36, 2001.
- [10] P.S. Heckbert, "Survey of Texture Mapping," *IEEE Computer Graphics and Applications*, vol. 6, no. 6, pp. 56-67, Nov. 1986.
- [11] P.S. Heckbert, "Fundamentals of Texture Mapping and Image Warping," master's thesis, Univ. of California, Berkeley, 1989.
- [12] H. Hoppe, "View-Dependent Refinement of Progressive Meshes," *Proc. SIGGRAPH '97*, pp. 189-198, 1997.
- [13] W. Stürzlinger, "Imaging All Visible Surfaces," UNC Computer Science Technical Report TR98-010, Univ. of North Carolina, Mar. 1998.
- [14] R. Pito, "A Solution to the Next Best View Problem for Automated Surface Acquisition," *IEEE Trans. Pattern Analysis and Machine Intelligence*, vol. 21, no. 10, pp. 1016-1030, Oct. 1999.
- [15] M. Wand, M. Fischer, I. Peter, F. Meyer auf der Heide, W. Straßer, "The Randomized z-Buffer Algorithm: Interactive Rendering of Highly Complex Scenes," *Proc. SIGGRAPH 2001*, pp. 361-370, 2001.
- [16] S.E. Chen and L. Williams, "View Interpolation for Image Synthesis," *Proc. SIGGRAPH '93*, pp. 270-288, 1993.
- [17] S. Fleishman, D. Cohen-Or, and D. Lischinski, "Automatic Camera Placement for Image-Based Modeling," *Proc. Pacific Graphics '99*, pp. 12-20, 1999.
- [18] L. Williams, "Pyramidal Parametrics," *Computer Graphics (SIGGRAPH '83 Proc.)*, vol. 17, pp. 1-11, July 1983.
- [19] P.H. Lin and T.Y. Lee, "The Camera Sampling Field," *Proc. 1999 Nat'l Computer Symp. (NCS '99)*, pp. 398-405, 1999 (in Chinese).
- [20] E. Kreyszig, *Advanced Engineering Mathematics*, fifth ed. Wiley, 1983.
- [21] P.H. Lin and T.Y. Lee, "Splatting Footprint Size Evaluation for Image-Based Rendering Using Camera Sampling Field," *Proc. Int'l Conf. Distributed Multimedia Systems*, pp. 95-100, 2001.
- [22] P. Heckbert, "Texture Mapping Polygons in Perspective," NYIT Computer Graphics Lab Technical Memo #13, 1983.
- [23] V. Popescu, A. Lastra, D. Aliaga, and M. de Oliveira Neto, "Efficient Warping for Architectural Walkthroughs Using Layered Depth Images," *Proc. IEEE Visualization '98*, pp. 211-215, Oct. 1998.



Ping-Hsien Lin received the BS degree in mechanical engineering and the MS degree in computer engineering from National Cheng-Kung University, Taiwan, in 1993 and 1998, respectively. He is currently working toward the PhD degree in the Department of Computer Science and Information Engineering, National Cheng-Kung University. His research interests include computer graphics, computer vision, image-based rendering.



Tong-Yee Lee received the BS degree in computer engineering from Tatung Institute of Technology in Taipei, Taiwan, in 1988, the MS degree in computer engineering from National Taiwan University in 1990, and the PhD degree in computer engineering from Washington State University, Pullman, in May 1995. Now, he is a professor in the Department of Computer Science and Information Engineering at National Cheng-Kung University in Tainan, Taiwan, Republic of China. He served as a guest associate editor for the *IEEE Transactions on Information Technology in Biomedicine* from 2000 to 2003. His current research interests include computer graphics, image-based rendering, visualization, virtual reality, surgical simulation, distributed and collaborative virtual environment. He leads a Computer Graphics Group/Visual System Lab at National Cheng-Kung University (<http://couger.csie.ncku.edu.tw/~vr>). He is a member of the IEEE.

► For more information on this or any computing topic, please visit our Digital Library at www.computer.org/publications/dlib.